

## Electrochemistry at Edge of Single Graphene Layer in a Nanopore

Shouvik Banerjee, Jiwook Shim, Jose Rivera, Xiaozhong Jin, David Estrada, Vita Solovyeva, Xiuque You, James Pak, Eric Pop, Narayana Aluru, and Rashid Bashir

ACS Nano, **Just Accepted Manuscript** • DOI: 10.1021/nn305400n • Publication Date (Web): 18 Dec 2012

Downloaded from <http://pubs.acs.org> on December 20, 2012

### Just Accepted

“Just Accepted” manuscripts have been peer-reviewed and accepted for publication. They are posted online prior to technical editing, formatting for publication and author proofing. The American Chemical Society provides “Just Accepted” as a free service to the research community to expedite the dissemination of scientific material as soon as possible after acceptance. “Just Accepted” manuscripts appear in full in PDF format accompanied by an HTML abstract. “Just Accepted” manuscripts have been fully peer reviewed, but should not be considered the official version of record. They are accessible to all readers and citable by the Digital Object Identifier (DOI®). “Just Accepted” is an optional service offered to authors. Therefore, the “Just Accepted” Web site may not include all articles that will be published in the journal. After a manuscript is technically edited and formatted, it will be removed from the “Just Accepted” Web site and published as an ASAP article. Note that technical editing may introduce minor changes to the manuscript text and/or graphics which could affect content, and all legal disclaimers and ethical guidelines that apply to the journal pertain. ACS cannot be held responsible for errors or consequences arising from the use of information contained in these “Just Accepted” manuscripts.



# Electrochemistry at Edge of Single Graphene Layer in a Nanopore

Shouvik Banerjee<sup>1,2,‡</sup>, Jiwook Shim<sup>2,3,‡</sup>, Jose Rivera<sup>2,4</sup>, Xiaozhong Jin<sup>5,6</sup>, David Estrada<sup>2,3</sup>, Vita Solovyeva<sup>2,3</sup>, Xiuque You<sup>7</sup>, James Pak<sup>7</sup>, Eric Pop<sup>2,3,6</sup>, Narayana Aluru<sup>5,6</sup>, Rashid Bashir<sup>2,3,4,★</sup>

<sup>1</sup>Department of Materials Science and Engineering, <sup>2</sup>Micro and Nanotechnology Laboratory,

<sup>3</sup>Department of Electrical and Computer Engineering, <sup>4</sup>Department of Bioengineering,

<sup>5</sup>Department of Mechanical Science and Engineering,

<sup>6</sup>Beckman Institute for Advanced Science and Technology,

University of Illinois at Urbana – Champaign, Urbana, IL, USA 61801

<sup>7</sup>School of Electrical Engineering, Korea University, Seoul, Korea

‡authors contributed equally

★ Corresponding author

[rbashir@illinois.edu](mailto:rbashir@illinois.edu)

## 1 **Abstract**

2 We study the electrochemistry of single layer graphene edges using a nanopore-based structure  
3 consisting of stacked graphene and Al<sub>2</sub>O<sub>3</sub> dielectric layers. Nanopores, with diameters ranging  
4 from 5 to 20 nm, are formed by an electron beam sculpting process on the stacked layers. This  
5 leads to unique edge structure which, along with the atomically thin nature of the embedded  
6 graphene electrode, demonstrates electrochemical current densities as high as  $1.2 \times 10^4$  A/cm<sup>2</sup>.  
7 The graphene edge embedded structure offers a unique capability to study the electrochemical  
8 exchange at an individual graphene edge, isolated from the basal plane electrochemical activity.  
9 We also report ionic current modulation in the nanopore by biasing the embedded graphene  
10 terminal with respect to the electrodes in the fluid. The high electrochemical specific current  
11 density for a graphene nanopore-based device can have many applications in sensitive chemical  
12 and biological sensing, and energy storage devices.

## 13 **Keywords**

14 Nanopores, graphene, graphene electrochemistry, nano-bio sensors, stacked graphene

15  
16 Graphene has attracted tremendous interest in the scientific world over the recent years due to its  
17 unique electronic,<sup>1-2</sup> thermal<sup>3</sup> and optical<sup>4</sup> properties. It has shown great promise in the field of  
18 electronics, biological and chemical sensing, and energy storage applications.<sup>5-6</sup> Studies on  
19 graphene electrochemistry have suggested the ability of graphene based electrodes to carry a  
20 large amount of current at electron transfer rates superior to graphite and carbon nanotube  
21 (CNT) electrodes.<sup>5</sup> The relative abundance of carbon on earth combined with widespread  
22 knowledge of carbon-based chemistries and stability makes the study of graphene based  
23 electrochemistry extremely exciting.<sup>5,7-8</sup>

1  
2  
3 1 Graphene is a single atom thick sheet of  $sp^2$  hybridized carbon atoms arranged in a honeycomb  
4  
5 2 lattice structure. A graphene sheet has two types of electron transfer sites – edge and basal. Edge  
6  
7 3 sites have already been demonstrated to possess enhanced electron transport rates and reactivity  
8  
9 4 in studies of CNT ends.<sup>9</sup> Graphene has a higher theoretical specific surface area (2630 m<sup>2</sup>/g) than  
10  
11 5 graphite and CNTs (1315 m<sup>2</sup>/g) and provides motivation for study of heterogeneous electron  
12  
13 6 transfer rates.<sup>8</sup> In addition, graphene can carry significant current densities without degradation  
14  
15 7 from electro-migration which typically causes significant damage in ultrathin metal films.<sup>10</sup>  
16  
17 8 Current densities as high as  $2 \times 10^9$  A/cm<sup>2</sup> have been reported for nanoscale interconnects based  
18  
19 9 on graphene grown by chemical vapour deposition (CVD).<sup>11</sup> The graphene edge plane atoms  
20  
21 10 have been reported to have significantly higher electron transfer rate compared to basal planes in  
22  
23 11 electrochemical studies on both highly ordered pyrolytic graphite as well as on multiple layers of  
24  
25 12 graphene.<sup>12-13</sup> Graphene modified glassy carbon electrodes have been reported to have much  
26  
27 13 greater electrochemical response, than unadulterated glassy carbon electrodes, to molecules like  
28  
29 14 paracetamol, hydrazine, glucose, ethanol dopamine as well as heavy metals.<sup>7,8</sup> Zhou *et al.*<sup>14</sup>  
30  
31 15 demonstrated the ability of chemically reduced graphene oxide electrodes to distinguish the  
32  
33 16 electrochemical current signal from the four bases of DNA, which could not be distinguished  
34  
35 17 with graphite and glassy carbon electrodes. Another important application of graphene  
36  
37 18 electrochemistry is in energy storage devices. The specific capacitance of chemically modified  
38  
39 19 graphene was found to be up to 1352 F/g,<sup>5</sup> and extremely high energy densities up to 85.6 Wh/kg  
40  
41 20 at room temperature have been reported.<sup>15-16</sup> Furthermore, graphene and hybrid graphene based  
42  
43 21 electrodes have been used to increase specific capacities of Li<sup>+</sup> ion based batteries, improving  
44  
45 22 power density and cyclic performance, while maintaining mechanical integrity at high current  
46  
47 23 densities.<sup>6</sup>  
48  
49  
50  
51  
52  
53  
54  
55  
56  
57  
58  
59  
60

1  
2  
3 1 Despite extensive studies on graphene sheets and graphene doped electrodes, the electrochemical  
4  
5 2 properties of isolated graphene edges remain relatively unexplored. Here, we demonstrate a  
6  
7 3 graphene edge embedded nanopore (GEEN) structure to isolate graphene edge electrochemical  
8  
9 4 activity from basal plane activity. Transmission electron microscopy (TEM) based sculpting  
10  
11 5 offers potential for control on graphene edge structures.<sup>17</sup> Furthermore, we demonstrate the use  
12  
13 6 of the embedded graphene edge to modulate the ionic flux in the nanopore. Along with a  
14  
15 7 conductive graphene terminal of thickness equivalent to the distance between two adjacent base  
16  
17 8 pairs in dsDNA (~0.34 nm), this could provide a basis for single DNA molecule analysis with  
18  
19 9 measurement methodologies like tunnelling or electrochemical redox reactions.  
20  
21  
22  
23

## 24 **Results and Discussion**

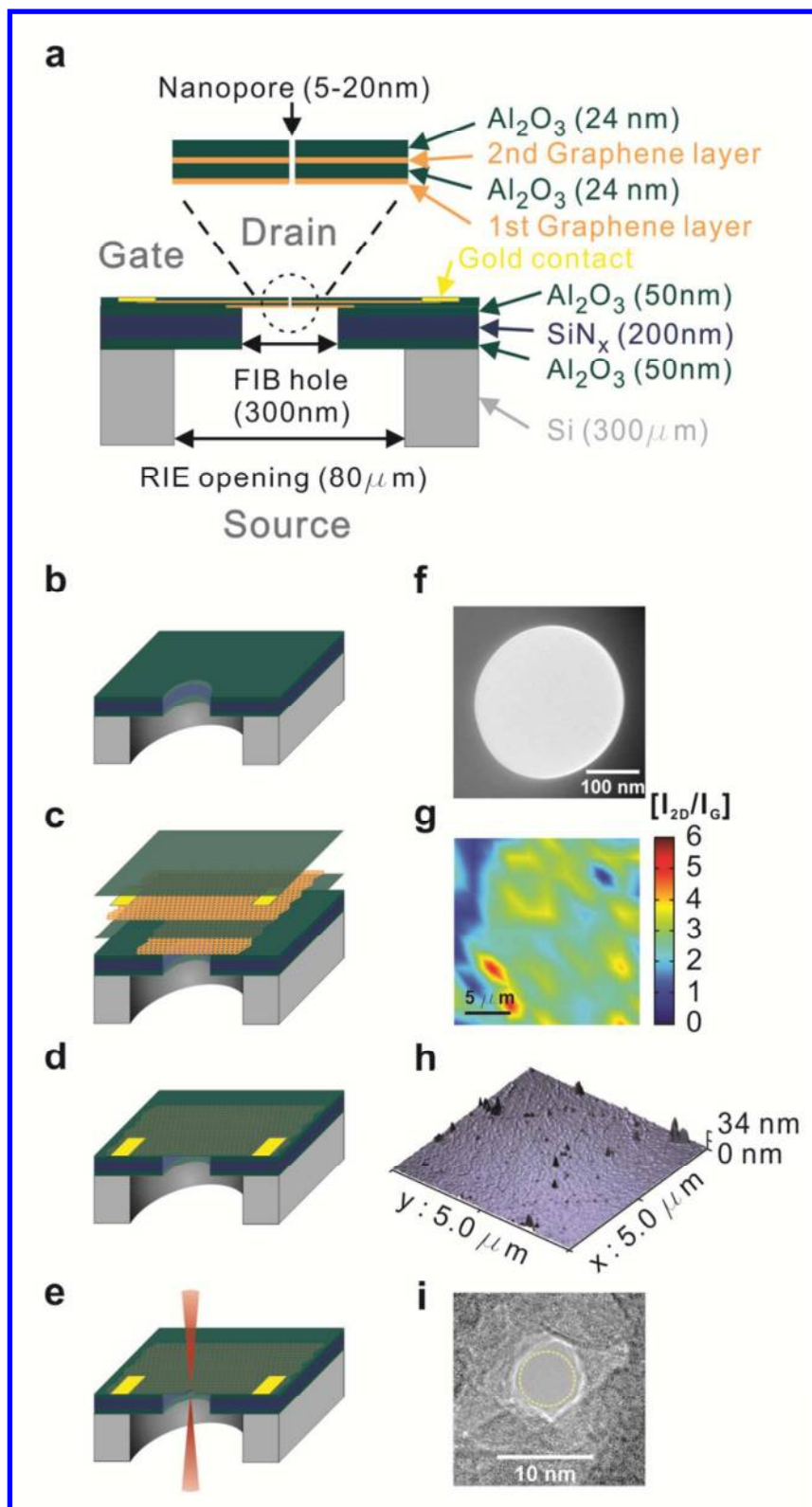
25  
26  
27 11 The fabrication of graphene nanopores using a TEM has been demonstrated previously and used  
28  
29 12 to sense biomolecules like polynucleotides and DNA protein complexes.<sup>18-19</sup> In this study, we  
30  
31 13 fabricate GEENs in stacked graphene and dielectric layers using a focused electron beam in a  
32  
33 14 TEM (200 keV), and measure the electrochemical current exchange at the graphene edge  
34  
35 15 embedded within the nanopore. The top Al<sub>2</sub>O<sub>3</sub> dielectric layer isolates the electrochemical basal  
36  
37 16 plane activity. We demonstrate the very high electrochemical current density as well as the first  
38  
39 17 known study of electrochemical current exchange at graphene (potentially as thin as single layer)  
40  
41 18 edge in an ionic solution. The combination of non-linear diffusion at nanoscale electrodes, an  
42  
43 19 enhanced concentration gradient of ions in the vicinity of the nanopore<sup>20</sup> and high electron  
44  
45 20 transfer rates at damaged edges of graphene<sup>12</sup> creates a unique system with high electrochemical  
46  
47 21 current densities.  
48  
49  
50  
51  
52

53 22 The schematic of our test GEEN structures is shown in Fig. 1a.<sup>21</sup> The fabrication process is  
54  
55 23 further described in Fig. 1b-e (details in the Methods section). Initially, a suspended hydrophilic  
56  
57  
58  
59  
60

1 supporting membrane of stacked layers of 50 nm Al<sub>2</sub>O<sub>3</sub>, 200 nm SiN<sub>x</sub> and 50 nm Al<sub>2</sub>O<sub>3</sub> is  
2 fabricated using deep reactive ion etching (DRIE). Subsequently, a hole of 300 ± 40 nm is  
3 formed in the supporting membrane using a focused ion beam (FIB) (Fig. 1b). The graphene –  
4 Al<sub>2</sub>O<sub>3</sub> stack is then formed on the supporting membrane with the FIB hole by transferring  
5 graphene films grown by CVD (details in the Methods section). We note that the hydrophilic  
6 nature of the supporting membrane helps spread the water more evenly during the graphene  
7 transfer steps and improves the smoothness of the transferred graphene/PMMA stack.<sup>22</sup> The  
8 Raman spectroscopy maps of the graphene 2D to G peak intensity ratios (I<sub>2D</sub>/I<sub>G</sub>) (Fig. 1g and  
9 Supplementary Fig. 4a-b) and the full-width at half maximum of the 2D peak (FWHM<sub>2D</sub>)<sup>23</sup>  
10 (Supplementary Fig. 4e-f) show our growth process results in a mix of monolayer and bilayer  
11 graphene, similar to our previous work.<sup>21</sup> The first graphene layer (G1) in our stack spans the  
12 FIB hole and acts as a mechanical support for deposition of the subsequent graphene and  
13 dielectric layers of our architecture. We note that subsequent to the graphene transfers, the  
14 membranes are annealed in an Ar/H<sub>2</sub> atmosphere at 400 °C to remove PMMA residue remnant  
15 from the transfer process.<sup>24</sup>

16 To ensure uniform nucleation of the subsequent Al<sub>2</sub>O<sub>3</sub> deposition (D1) onto the chemically inert  
17 graphene basal planes, a metallic seed layer of Al (2 nm thick) is evaporated onto the graphene.<sup>25</sup>  
18 Al<sub>2</sub>O<sub>3</sub> is a suitable choice as the dielectric due to its excellent mechanical stability<sup>26</sup> and  
19 reduction in 1/f noise compared to Si<sub>3</sub>N<sub>4</sub> and SiO<sub>2</sub> membranes.<sup>27-28</sup> The atomic force microscopy  
20 (AFM) images (Fig. 1h and Supplementary Fig. 4d) clearly show dense and uniform deposition  
21 of the dielectric due to the presence of the seed layer (Supplementary Fig. 5a-c and  
22 Supplementary Fig. 7) as compared to dielectric deposition without the Al seed layer  
23 (Supplementary Fig. 5a-b). ALD is chosen as it offers sub nanometer control over dielectric

1 thickness in addition to being a conformal deposition technique and a low temperature process,  
2 making it compatible with the previously transferred graphene layers.<sup>21</sup> The thickness of the  
3 dielectric deposited is 24 nm, a value established through extensive leakage testing in fluidic  
4 environments (Fig. 2 and Supplementary Fig. 1). Similar thicknesses of dielectric have been  
5 reported to provide effective isolation in ionic fluid environments in transistor based devices.<sup>29-30</sup>  
6 A second graphene layer (G2) is transferred onto D1 and annealed in an Ar/H<sub>2</sub> atmosphere. This  
7 layer is contacted using Ti/Au contacts and insulated by depositing another 24 nm of Al<sub>2</sub>O<sub>3</sub> (D2)  
8 as described above (Details in the Methods section).





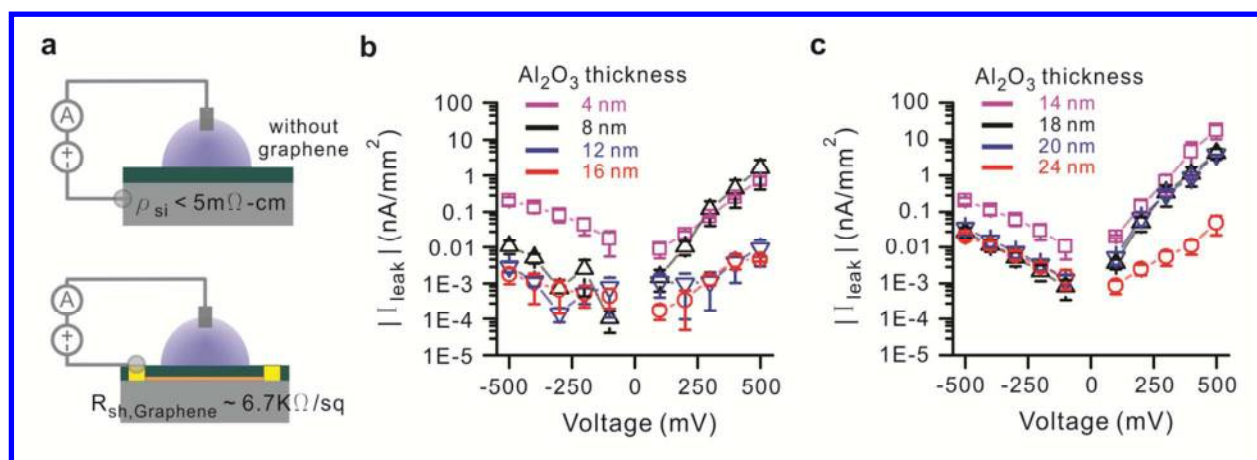
1 Figure 1. Schematic diagram of graphene-embedded stacked membrane structure and fabrication.  
2 (a) Schematic showing the thickness of each layer as well as diameters of RIE, FIB and nanopore  
3 holes (b) Supporting membrane consists of three layers of 50 nm of Al<sub>2</sub>O<sub>3</sub>, 200 nm of SiN<sub>x</sub> and  
4 50 nm of Al<sub>2</sub>O<sub>3</sub>, deposited on 300 μm-thick double polished prime Si wafer. RIE is used to etch  
5 80 μm-wide opening in Si wafer to supporting membrane and 300 nm through hole is fabricated  
6 in supporting membrane by FIB. (c) First graphene layer transferred onto the FIB hole acts as the  
7 support for subsequent layers. This is insulated from the second graphene layer by 24 nm of  
8 Al<sub>2</sub>O<sub>3</sub> deposition. Second graphene layer, which is the active electrode at the middle of  
9 membrane, is transferred onto first Al<sub>2</sub>O<sub>3</sub> layer. Ti/Au deposition enables the formation of  
10 contacts. A further layer of Al<sub>2</sub>O<sub>3</sub> is deposited to insulate the electrode from the ionic solution.  
11 (d) Final structure of graphene embedded membrane suspended on 300 nm FIB hole. (e) Focused  
12 electron beam (CBED mode) in TEM is used to fabricate a single nanopore of 5 to 20 nm  
13 diameter. (f) TEM image of FIB hole of 300 nm diameter in supporting membrane. (g) Raman  
14 spectroscopy of I<sub>2D</sub> / I<sub>G</sub> obtained from graphene surface indicating predominantly monolayer  
15 coverage. (h) AFM image of membrane surface. Roughness (Ra = 1.89 ± 0.67 nm) is  
16 significantly reduced on deposition of Al<sub>2</sub>O<sub>3</sub> on graphene compared to bare graphene surface (Ra  
17 = 0.84 ± 0.21 nm). (i) 5nm nanopore is fabricated by convergent electron beam in TEM.

18  
19 To explore the electrochemical current exchange at the graphene nanopore edges, it is essential  
20 to eliminate current exchange at the basal plane from affecting our measurements. In the  
21 embedded graphene membrane, the parasitic leakage current from gate to source and gate to  
22 drain (indicated in Fig. 1a) could adversely affect our experimental values. The active device  
23 area exposed to fluid on the backside (gate-source path) is just the area exposed to the FIB hole

1 of 300 nm. This area is insulated from the fluid by the 24 nm  $\text{Al}_2\text{O}_3$  under the graphene gate  
2 electrode. The rest of the graphene is well insulated by a total thickness of 300nm of stacked  
3  $\text{Al}_2\text{O}_3$  and  $\text{SiN}_x$  layers of the supporting membrane structure. On the gate-drain path the entire  
4 encapsulated graphene sheet is shielded from the fluid by just the top layer of 24 nm  $\text{Al}_2\text{O}_3$ . The  
5 fluid area exposed at the top layer corresponds to the area exposed by the o-rings (diameter =  
6 1.42 mm) used to seal the fluidic setup. To mimic our device structure and characterize leakage  
7 through the top dielectric, we fabricated the device as shown in Fig. 2 a. We compared the  
8 leakage current through different thicknesses of  $\text{Al}_2\text{O}_3$  deposited on a bare conductive silicon  
9 wafer and  $\text{Al}_2\text{O}_3$  deposited on a graphene sheet transferred onto an  $\text{Al}_2\text{O}_3$  coated (on Si wafer)  
10 top surface, similar to the D1/G2/D2 stack of our actual devices. The ALD dielectric deposition  
11 of  $\text{Al}_2\text{O}_3$  on graphene is preceded by the seed layer Al (~ 2 nm thick) evaporation as described  
12 previously. The leakage is measured by attaching a PDMS well (2.75 mm in diameter) on top of  
13 the device to hold the fluid. The current is measured between the graphene electrode and  
14 Ag/AgCl electrode dipped in the electrolyte fluid. All leakage measurements were performed  
15 with a 1 M KCl solution. The conductive silicon and the graphene electrode are connected to  
16 ground in all measurements.

17 The leakage densities observed are presented on a logarithmic scale (absolute value) in Fig. 2 b-  
18 c. On the bare silicon wafer, a slight asymmetry was observed in the I-V characteristics. For a  
19 positive Ag/AgCl electrode voltage a higher leakage current density was observed through the  
20 dielectric. The leakage current density reduces from -0.2 to -0.001  $\text{nA}/\text{mm}^2$  at -500 mV, as the  
21 dielectric thickness is increased from 4 to 16 nm. Comparing these values to leakage currents on  
22 samples with the dielectric deposited on graphene we can see a significant increase in the  
23 leakage current of the latter (Fig. 2c). The electrochemical exchange at the dielectric-electrolyte

1 interface has been reported in electrolyte-oxide-silicon (EOS) devices.<sup>31</sup> Since the leakage  
 2 current is high at positive electrode voltages, this could indicate electron tunnelling through the  
 3 pinholes in the dielectric as shown in our AFM images (Supplementary Fig. 4d and  
 4 Supplementary Fig. 9), similar to those reported in TiO<sub>2</sub> coated CVD graphene membranes.<sup>18</sup> On  
 5 the other hand, at negative electrode voltages the leakage currents are significantly suppressed in  
 6 the voltage range from 0 to -500 mV. Increasing the dielectric thickness from 14 to 24 nm  
 7 decreases the leakage current density from -0.2 to -0.02 nA/mm<sup>2</sup>. For a 2.75 mm diameter PDMS  
 8 well, that translates to a current of about 118.7 pA. Since the ionic current through the nanopore  
 9 is usually in the range of nanoamperes, at least one order of magnitude lower leakage current is  
 10 essential to maintain reliability of our electrochemical current measurements and to have gate  
 11 current independent from interference due to leakages. Therefore, we use only the negative  
 12 voltage range (0 to -500 mV) in our nanopore measurements to minimize and avoid leakage  
 13 across D2.



14  
 15 Figure 2. Leakage test on various thickness of Al<sub>2</sub>O<sub>3</sub>. (a-top) Schematics showing leakage  
 16 measurement setup for Al<sub>2</sub>O<sub>3</sub> on p++ Silicon ( $\rho < 5 \text{ m}\Omega\text{-cm}$ ). Al<sub>2</sub>O<sub>3</sub> of thickness 4 to 16 nm were  
 17 deposited on the conductive Si wafer. Measurements are conducted with one electrode connected

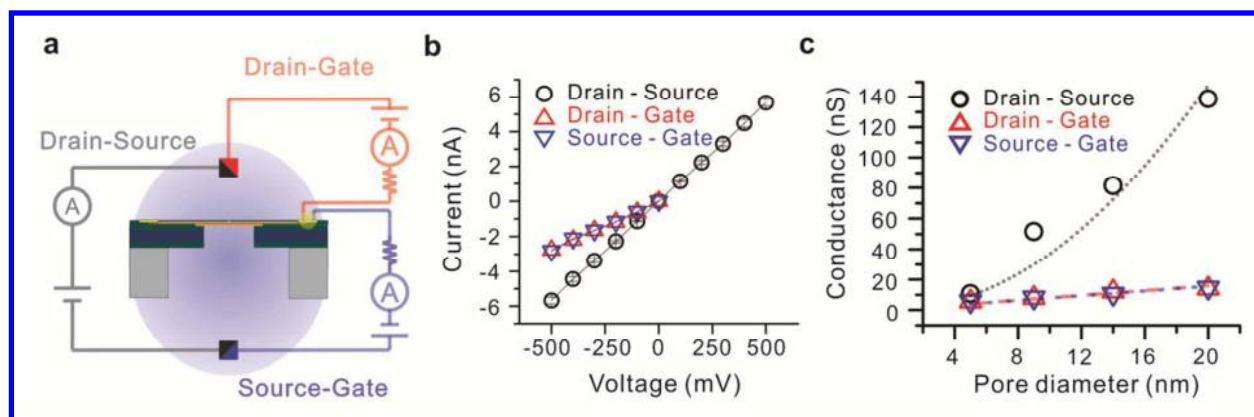
1  
2  
3 1 to Si wafer and the other attached to Ag/AgCl electrode in the solution (a-bottom) Schematic of  
4  
5 2 leakage measurement setup for Al<sub>2</sub>O<sub>3</sub> on graphene transferred onto Si surface with Al<sub>2</sub>O<sub>3</sub>  
6  
7 3 deposited on top. Al<sub>2</sub>O<sub>3</sub> thickness in range of 14 to 24 nm is deposited on graphene ( $R_{sh} \approx 6.7$   
8  
9 4 k $\Omega$ /sq) transferred on Si wafer with a ALD deposited Al<sub>2</sub>O<sub>3</sub> top surface. Measurements are  
10  
11 5 conducted between the graphene film contacted with aluminium wires and the solution contacted  
12  
13 6 with Ag/AgCl electrodes. All leakage experiments are performed in 1 M KCl, 10 mM Tris, 1  
14  
15 7 mM EDTA at pH 7.6 and at room temperature ( $22 \pm 2$  °C). (b) Leakage current density measured  
16  
17 8 for Al<sub>2</sub>O<sub>3</sub> on conductive Silicon. Al<sub>2</sub>O<sub>3</sub> thickness less than 10 nm showed leakage current greater  
18  
19 9 than 1 nA/mm<sup>2</sup> at 500 mV, but thicker Al<sub>2</sub>O<sub>3</sub> (>10 nm) showed much greater insulation over the  
20  
21 10 voltage range of -500 mV to +500 mV. (c) Leakage current density for Al<sub>2</sub>O<sub>3</sub> deposited on  
22  
23 11 graphene. Leakage current is observed to be fairly high up to 20 nm-thick Al<sub>2</sub>O<sub>3</sub>. Also the  
24  
25 12 leakage is significantly higher for positive voltage at Ag/AgCl electrode. 24 nm-thick Al<sub>2</sub>O<sub>3</sub>  
26  
27 13 displays decent insulation from leakage. Current leakage occurrence at relative thicker Al<sub>2</sub>O<sub>3</sub>  
28  
29 14 deposited on graphene is associated with wrinkles on graphene (Supplementary Fig. 9).  
30  
31  
32  
33  
34  
35  
36  
37  
38

39 16 On settling upon a dielectric thickness of 24 nm, nanopores are drilled in this stacked structure  
40  
41 17 using convergent beam electron diffraction (CBED) mode in a TEM (Fig. 1e and 1i). We  
42  
43 18 fabricated four different pore diameters (5, 9, 14, 20 nm) for our test structures. For a 5nm pore,  
44  
45 19 the beam sputters through the membrane in about 30s. For larger pores, sculpting is needed by  
46  
47 20 moving the beam on the edges of the pore to expand it. Control is achieved by in-situ monitoring  
48  
49 21 of the nanopore dimension with imaging. Since TEM provides angstrom level precision we  
50  
51 22 believe the nanopore dimensions are accurate within a tolerance of 1nm. Prior to assembly in the  
52  
53 23 fluidic setup the backside (silicon trench side) (Fig. 1a) is O<sub>2</sub> plasma treated to make the pore  
54  
55  
56  
57  
58  
59  
60

1 hydrophilic to facilitate wetting.<sup>18,21</sup> The top graphene layer (G2) is contacted and the chip is  
2 encapsulated in a custom built fluidic setup (Supplementary Fig. 6). Ethanol is then flushed into  
3 both chambers to promote wetting as reported in previous nanopore studies.<sup>19,21</sup> The ethanol is  
4 flushed away repeatedly with de-ionized (DI) water and the desired buffer solution is inserted  
5 into both chambers.

6 The schematics of drain-source, drain-gate and source-gate measurements are shown in Fig. 3a.  
7 An external resistor of 20 M $\Omega$  is placed in series with graphene. This helps ensure our graphene  
8 current measurements are not significantly affected by leakage. At 500 mV a 20 M $\Omega$  resistor  
9 conducts 25 nA of current. Since the currents observed are much less it indicates the  
10 electrochemical resistance at the graphene edge terminal is much higher and determines current  
11 in the series circuit. For a 1 M KCl solution used in these measurements, the drain-source  
12 conductance exhibits a squared dependence<sup>32</sup> with pore diameter as indicated in Fig. 3c. The  
13 current values for the different pore diameters also seem to be in good agreement with our  
14 previous work on similar structures.<sup>21</sup> For the source-gate and drain-gate measurements, the  
15 graphene gate is always connected to ground to maintain a positive voltage with respect to  
16 source or drain and ensure minimal leakage in accordance to our leakage measurements as  
17 described earlier. This is indicated in the I-V curves for a 5 nm pore showed in Fig. 3b (and  
18 Supplementary Fig. 2). The drain-gate and source-gate conductance is also plotted in Fig. 3c and  
19 is observed to be nearly identical for each of the four different pores diameters, indicating that  
20 the measured current is indeed only through the electrochemical exchange at the graphene  
21 terminal and the leakage contribution to these measurements on the drain side is indeed  
22 negligible. The o-rings used in these experiments are approximately  $1.42 \pm 0.1$  mm in diameter.  
23 Based on the leakage measurements, for a 24 nm thick Al<sub>2</sub>O<sub>3</sub> insulation layer, the maximum

1 contribution of leakage at drain/source at potential of -500 mV should be approximately 30 pA,  
2 which is about two orders of magnitude less than the currents observed in these measurements.  
3 This is further confirmed by similar measurements in the same structure without a nanopore as  
4 currents in the range of 10 to 20 pA are observed across all three terminals. Furthermore, the  
5 conductance through the graphene terminal scales fairly linearly with pore diameter as seen in  
6 Fig. 3c. The slight variation from the linear dependence can be explained from the varying  
7 graphene sheet thickness (Fig. 1b) over the membrane, which affects pore sidewall area, since  
8 the pore region could consist of a mixture of mono and bi-layer graphene. Nonetheless, we do  
9 see an increase of conductance from 5 to 15 nS as the pore diameter is increased from 5 to 20  
10 nm. This is expected and indeed proves that this current is due to electrochemical exchange on  
11 the cylindrical pore sidewalls.



12  
13 Figure 3. Electrochemical measurements for embedded graphene nanoelectrode. (a) Schematic  
14 diagram of measurement setup. For the drain-source measurement (gray), source is connected to  
15 ground and voltage applied at the drain. For drain-gate (red) and drain-source (blue)  
16 measurements, the gate is connected to ground and voltage is applied to the other terminal. (b)  
17 Current-voltage curve of nanopore ionic current and electrochemical behavior of graphene edge  
18 through 5 nm nanopore. Identical currents through the drain-gate and source-gate pathways

1 indicate electrochemical exchange at the exposed graphene edge. (c) Conductance dependence  
2 on pore diameter. Drain-source conductance shows a square dependence on pore diameter, while  
3 gate current exchange shows a fairly linear dependence on pore diameter consistent with  
4 electrochemical exchange at cylindrical nanopore wall. The slight variation from linear  
5 dependence is may be attributed to varying graphene sheet thickness on various regions of the  
6 membrane. 5, 9, 14 and 20 nm diameter nanopores were used in this study. All experiments are  
7 performed in 1 M KCl, 10 mM Tris, 1 mM EDTA at pH 7.6

8  
9 From the current values of electrochemical exchange at the 5nm pore edge, (Fig. 3b) and  
10 assuming a predominantly monolayer coverage of graphene, we calculate a current density of up  
11 to  $1.2 \times 10^4$  A/cm<sup>2</sup> at a drain voltage of -200mV. This current density is three orders of  
12 magnitude higher than electrochemical current densities reported for oxygen reduction on CNT  
13 electrodes.<sup>29</sup> From electrochemistry studies on basal planes of individual monolayer sheets for  
14 CVD-grown graphene reported by Li *et al.*,<sup>33</sup> a current density of about  $6 \times 10^{-8}$  A/cm<sup>2</sup> is  
15 obtained. Thus a significant electrochemical current enhancement is observed using individual  
16 graphene edges as the active electrode material. Furthermore, we simulated the concentration of  
17 H<sup>+</sup> and Cl<sup>-</sup> ions at the nanopore (details in the Methods section) and the Cl<sup>-</sup> ions are significantly  
18 higher in number. Thus, all redox couples based on H<sup>+</sup>/OH<sup>-</sup> ions can safely be ignored as it is  
19 highly unlikely they can contribute to such high currents. Thus, we conclude that the reaction at  
20 the positive graphene electrode (anode) edge is the oxidation of Cl<sup>-</sup> ions. The equilibrium  
21 oxidation potential for this reaction at room temperature is -1.36 V.<sup>34</sup> However surface  
22 treatments enhancing the number of possible adsorption sites in diamond electrodes have been  
23 reported to lower the potential of chloride oxidation by as much as 0.5 V.<sup>35</sup> A similar mechanism

1 might explain high electron transfer rates observed on graphene edges at low voltages.  
2 Electrochemical studies on graphite edges have exhibited extremely high electrochemical  
3 reaction rates.<sup>12-13</sup> Fast electron transfer kinetics reported on CNTs are also attributed to tube  
4 ends, identified as the reactive sites.<sup>9,36-37</sup> For GEENs we expect all sites at the nanopore edge to  
5 be damaged. Girit *et al.*<sup>17</sup> reported TEM drilled graphene nanopores which reconstruct and  
6 eventually exhibit a zigzag edge configuration due to its higher stability. For a graphene  
7 nanoribbon with zigzag edges, a large peak in the density of states is observed at the edges,<sup>38-39</sup>  
8 as confirmed by Scanning tunnelling microscopy (STM) studies.<sup>40</sup> An enhancement in the  
9 density of states at the graphene nanopore edges of our architecture may have a direct effect in  
10 enabling the high electrochemical current densities observed in our measurements.

11 We note an electrochemical reaction consists of mass transport of the reactive species to the  
12 electrode surface and electron exchange at the electrode surface.<sup>41</sup> Since the dominant  
13 electrochemical exchange in our measurements occurs at the damaged graphene nanopore edges,  
14 it would appear that the electron exchange is not the rate limiting step. Diffusion limited  
15 electrochemical systems operate in the linear diffusion regime. For linear diffusion based  
16 systems, *i.e.* when the electro-active length is  $\approx$  comparable to the diffusion layer thickness, the  
17 reaction is diffusion limited and the peak current  $i_p$  is given by the Randles-Sevcik equation:<sup>9</sup>

$$i_p = 2.69 \times 10^5 n^{\frac{3}{2}} A C D^{\frac{1}{2}} \nu^{\frac{1}{2}} \quad (1)$$

18 where,  $n$  is the number of moles of electrons transferred in the reaction,  $A$  is the area of the  
19 electrode ( $\text{cm}^2$ ),  $C$  is the analyte concentration (in moles/ $\text{cm}^3$ ),  $D$  is the diffusion coefficient  
20 ( $\text{cm}^2/\text{s}$ ), and  $\nu$  is the scan rate (V/s) of the applied potential. For a chloride ion oxidation  
21 reaction  $n$  is assumed to be 1. The active area of the electrode is the cylindrical pore area, which  
22



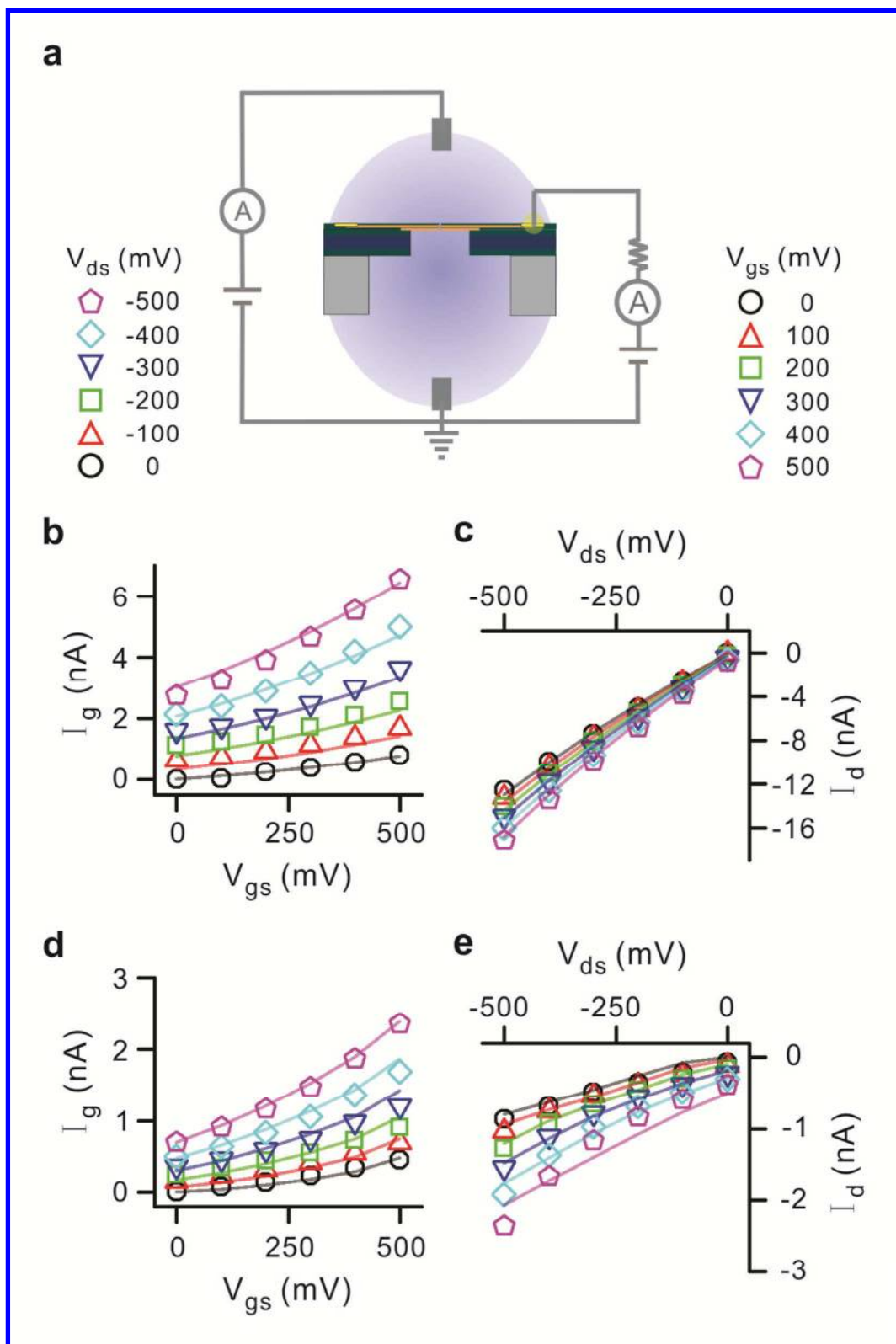
1 for a 5 nm pore, is calculated to be  $9.4 \times 10^{-14} \text{ cm}^2$ . The concentration is taken as  $10^{-3} \text{ mol/cm}^3$   
2 and the diffusion coefficient of  $\text{Cl}^-$  is taken as  $1.5 \times 10^{-5} \text{ cm}^2/\text{s}$ .<sup>42</sup> For a 5nm pore and a scan rate  
3 of 100 mV/10 s the peak current by the above equation gives  $i_p = 9.6 \times 10^{-7} \text{ nA}$ , which is much  
4 smaller than observed current. Thus the reaction is not diffusion limited. It should be noted that  
5 our electrode size is in nanometers and is much smaller than the diffusion layer thickness  
6 (usually of the order of  $\sqrt{Dt} = 3.8 \times 10^{-2} \text{ cm}$ ,<sup>43</sup> where  $t$  is the time period of each scan) and hence  
7 convergent diffusion effects are significant. For microelectrodes, convergent diffusion leads to  
8 significantly higher mass transport and thus higher current densities.<sup>9</sup> We believe that with the  
9 graphene nanoelectrodes used in our experiments, this effect would be exacerbated. Furthermore,  
10 the local concentration of the electro-active species ( $\text{Cl}^-$ ) is much higher and a threefold increase  
11 has been reported when compared to microelectrodes of same electro-active area. This increase  
12 in concentration is in the vicinity of the nanopore as compared to the bulk solution, also results in  
13 faster mass transport,<sup>20</sup> contributing to the large current densities measured in our GEEN  
14 structures. Our simulations report local (nanopore edge) concentration of  $\text{Cl}^-$  as high as 8.5 M for  
15 bulk KCl concentration of 1 M (details in the Methods section).

16 We further investigate the use of our structure as a 3 terminal device analogous to a transistor  
17 (Fig. 4a). The source terminal is always connected to ground in these measurements. The source  
18 current can be obtained by Kirchhoff's law

$$I_d = I_g + I_s \quad (2)$$

19 where,  $I_d$ ,  $I_g$  and  $I_s$  are the drain, gate and source currents respectively. In accordance with our  
20 leakage results, the drain is always kept at a negative potential with respect to the gate for  
21 minimal interference from leakage. The graphene gate current characteristics ( $I_g$  vs.  $V_{gs}$ ) for a 5  
22

1  
2  
3 1 nm pore in 1 M KCl solution are shown in Fig. 4b. A shift in the gate current values is observed  
4  
5  
6 2 as the drain voltage is swept from 0 to -500 mV at a sweep rate of 100 mV/10 s (step function).  
7  
8 3 Numerical simulations are used to explain gate current characteristics (details in the Methods  
9  
10 4 section). The  $I_g$  dependence on  $V_{gs}$  and  $V_{ds}$  voltage is estimated by an exponential function. This  
11  
12 5 equation is coupled with the Poisson-Nernst-Planck equation and the Grahame equation and  
13  
14 6 solved simultaneously to obtain both gate and drain current values. Fig. 4c shows the  $I_d$  vs  $V_{gs}$   
15  
16 7 characteristics. As expected, a shift in the  $I_d$  is seen as  $V_{gs}$  is swept. The simulation results are in  
17  
18 8 good agreement with the experimental data at 1 M KCl.  
19  
20  
21  
22  
23  
24  
25  
26  
27  
28  
29  
30  
31  
32  
33  
34  
35  
36  
37  
38  
39  
40  
41  
42  
43  
44  
45  
46  
47  
48  
49  
50  
51  
52  
53  
54  
55  
56  
57  
58  
59  
60



1

1  
2  
3 1 Figure 4. Three terminal measurement for the graphene embedded membrane. (a) Schematic  
4  
5 2 diagram with source connected to ground while voltage is swept at the drain and gate terminals.  
6  
7  
8 3 (b) and (d) Gate current characteristics for 1 M KCl and 10 mM KCl respectively. The variation  
9  
10 4 of gate current with gate source bias as drain voltage is varied is shown. The scatter points are  
11  
12 5 experimental numbers while the straight lines are simulation fits. (c) and (e) Drain current  
13  
14 6 characteristics for 1 M KCl and 10 mM KCl solution respectively. The variation of drain current  
15  
16 7 with drain source bias as gate voltage is varied is recorded. Both solutions are prepared with 10  
17  
18 8 mM Tris and 1 mM EDTA for buffering at pH 7.6.  
19  
20  
21  
22 9

23  
24 10 Further confirmation of observation of graphene edge currents is obtained by repeating these  
25  
26 11 measurements for three more pores of 9, 15 and 20 nm diameters (Fig. 5a). Since the measured  
27  
28 12 currents are due to electrochemical exchange at the pore walls, the active area is cylindrical.  
29  
30 13 Thus linear dependence of  $I_g$  on pore diameter is expected. We previously noted this in our two-  
31  
32 14 terminal measurements for currents due to electrochemical exchange at graphene electrodes (Fig.  
33  
34 15 3c). At 1 M KCl buffer solution the  $I_g$  values at two different  $V_{ds}$  (0 and -200 mV) are shown in  
35  
36 16 Fig. 5e and 5f, respectively, for  $V_{gs}$  swept between 0 to +500 mV. The simulated values (solid  
37  
38 17 lines) show excellent agreement with experimental data (symbols) for all four pore diameters.  
39  
40 18 We see a four-fold increase in the  $I_g$  value as the pore size is increased from 5 to 20 nm.  
41  
42  
43  
44  
45  
46  
47  
48  
49  
50  
51  
52  
53  
54  
55  
56  
57  
58  
59  
60

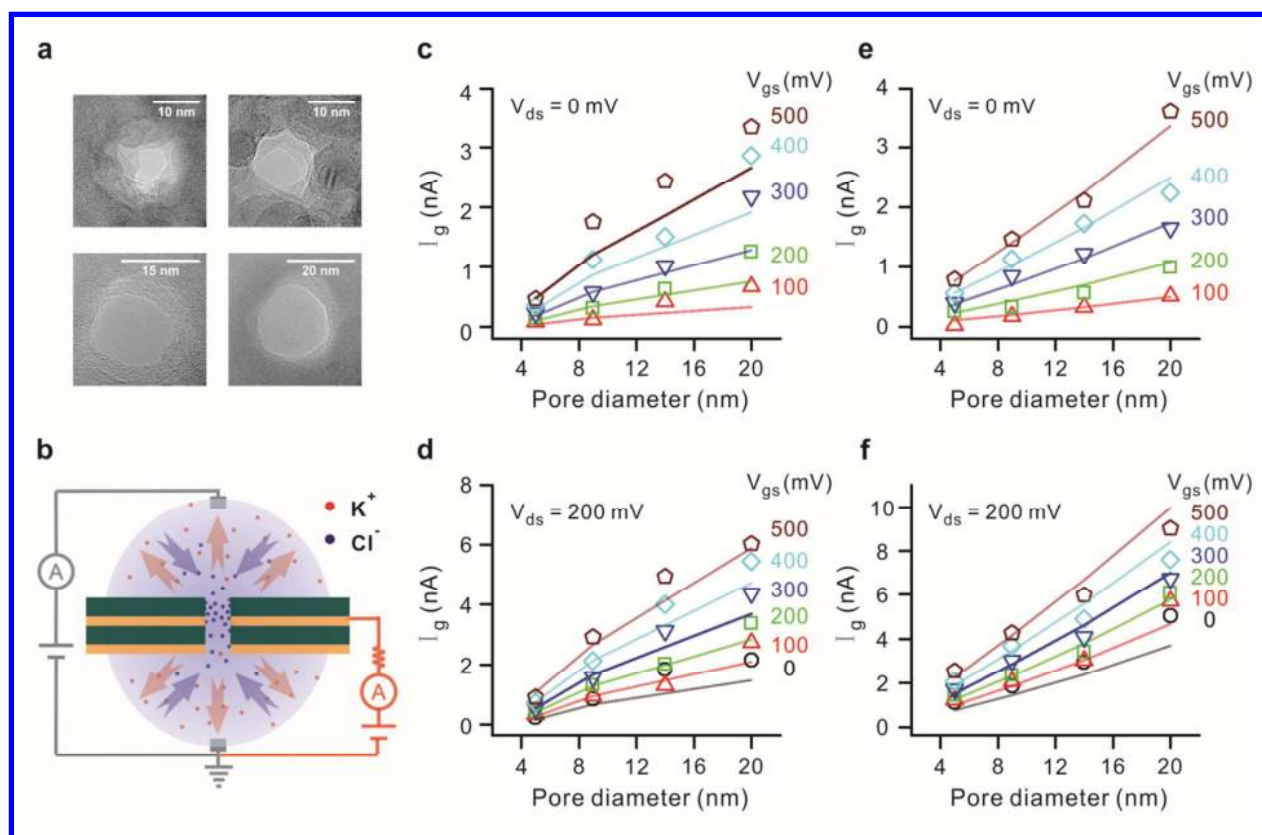


Figure 5. Gate current dependence on pore diameter (a) TEM images of nanopores of four different diameters (5, 9, 14, 20 nm) nanopores drilled through an embedded graphene membrane. (b) Schematic diagram of electrochemistry. The positive gate bias leads to attraction of chloride ions to the nanopore and expulsion of potassium ions. Red dots and arrows represent potassium ions while blue dots and arrows are for chloride ions. (c-f) Scaling of gate current with pore size at drain bias of 0 and -200 mV for 4 different pore diameters. (c), (d) Gate current dependence on pore diameter using 10 mM KCl solution. Linear dependence on pore diameter is observed over gate bias ranging from 0 to +500 mV for both drain bias values. (e), (f) Gate current dependence on pore diameter using 1 M KCl solution. Similar linear dependence on pore diameter is observed entire voltage range. The scatter points are experimental numbers while the

1  
2  
3 1 straight lines are simulation fits. Both solutions are prepared with 10 mM Tris and 1 mM EDTA  
4  
5  
6 2 for buffering at pH 7.6  
7

8 3  
9  
10 4 Similar experiments were repeated in the 10 mM KCl solution. The ( $I_g$  vs.  $V_{gs}$ ) and ( $I_d$  vs.  $V_{ds}$ )  
11  
12 5 characteristics show a similar shift as expected (Fig. 4d and 4e). The simulation results (solid  
13  
14 6 lines in both graphs) are in good agreement with the experimental results, although in this case  
15  
16 7 the fitting parameters are altered for a 5 nm pore since the pore diameter is smaller than the  
17  
18 8 Debye layer thickness (details in the Methods section).<sup>44</sup> The  $I_g$  values do not scale linearly with  
19  
20 9 concentration and this is attributed to enhanced ionic flux in the vicinity of the nanopore as  
21  
22 10 shown in our simulations (details in the Methods section). The pore diameter dependence  
23  
24 11 measurements in 10 mM KCl for all four pore diameters show fairly good agreement with  
25  
26 12 simulated results and a linear increase of  $I_g$  with pore diameter is displayed (Fig. 5c and 5d).  
27  
28 13 Note that the values of  $I_d$  and  $I_g$  are observed to be nearly the same for these measurements at  
29  
30 14 10mM, as illustrated in Supplementary Fig. 3. From equation (2), this implies an extremely low  
31  
32 15  $I_s$ .  
33  
34  
35  
36  
37

38 16 Our results confirm that the observation of electrochemical exchange at the graphene edge,  
39  
40 17 isolated from any basal plane activity. An array of GEENs could potentially be used to harness  
41  
42 18 extremely large value of energy density per unit mass. Methods like electron beam, nanoimprint  
43  
44 19 lithography or Helium based focused ion beam<sup>45</sup> techniques could be used to mass produce  
45  
46 20 arrays of nanopores. Improvement in dielectric coverage of graphene by use of other materials  
47  
48 21 like  $HfO_2$ <sup>46</sup> and different dielectric seed layer materials<sup>47</sup> like Titanium or 3,4,9,10-perylene  
49  
50 22 tetracarboxylic acid dianhydride (PTCDA) would significantly enhance the voltage range used in  
51  
52  
53  
54  
55  
56  
57  
58  
59  
60

1 these experiments by reducing parasitic leakage through the dielectric enabling higher current  
2 densities to be harnessed.

3 Furthermore, we note that the differential flux in ions on opposite sides of the nanopore could  
4 potentially have interesting applications in controlling the flux of bio-molecules to be sensed  
5 though electrochemical exchange at the graphene edge. The differential ion flow rate could  
6 potentially be used to trap molecules within the pore allowing for electrical interrogation using  
7 the conductive graphene terminal. Wanunu *et al.*<sup>48</sup> reported the use of salt gradients as a means  
8 to enhance DNA capture rate to increase throughput of the detection scheme. Another major  
9 biosensing application of an embedded conductive terminal in a solid state nanopore is with  
10 regards to DNA sequencing.<sup>49</sup> STM based studies have been demonstrated<sup>50</sup> to distinguish  
11 deoxynucleotide monophosphates (dNMPs) and partially sequence DNA oligomers by using  
12 tunnelling current measurements. Tsutsui *et al.*<sup>51-52</sup> demonstrated tunnelling current  
13 measurements to distinguish bases in deoxynucleotide triphosphate (dNTP) molecules. If an  
14 embedded conductive terminal, *e.g.* GEENs, can be combined with biological<sup>53</sup> or electronic<sup>54</sup>  
15 methods to slow DNA translocation rates, it could provide a pathway to DNA sequencing.

## 16 **Conclusion**

17 In summary, we present the investigation of electrochemical current exchange at a CVD-grown  
18 graphene edges within a nanopore. We demonstrate the ability of our graphene embedded  
19 nanopore structures to study electrochemistry at individual graphene layers in isolation from  
20 contribution from basal planes. We observed electrochemical current densities on the order of  
21  $10^4$  A/cm<sup>2</sup>, three orders of magnitude higher than those reported for carbon nanotubes and much  
22 higher than those reported for graphene surface electrochemical studies. The high currents are  
23 attributed to a combination of the nanopore edge structures produced by electron beam sculpting

1 along with the convergent diffusion mechanisms due to nanosized electrodes, which have been  
2 reported to enhance ionic flux of reactive species. We also demonstrated the modulation of ionic  
3 current by the use of the embedded conductive graphene terminal. Numerical simulations were  
4 performed to confirm the transistor like characteristics of the device. Extremely high  
5 electrochemical current densities have exciting applications for both chemical and biological  
6 sensing as well as energy storage. Scaling of these structures by producing arrays of nanopores  
7 could enable multiple applications.

## 8 **Experimental Details**

### 9 **Graphene Growth and Transfer:**

10 Graphene is grown by chemical vapor deposition (CVD) on 1.4 mil copper foils purchased from  
11 Basic Copper.<sup>21,24,55</sup> Copper foil is placed in an Atomate CVD system and annealed at ~1000 °C  
12 under Ar/H<sub>2</sub> flow for 90 minutes at a base pressure of ≈ 4.4 Torr. Graphene is grown for 30  
13 minutes at 1000 °C under 850 sccm of CH<sub>4</sub> and 50 sccm of H<sub>2</sub> at a base pressure of about 2.5  
14 Torr. The resulting graphene and Cu substrates are cooled to 400 °C under 850 sccm of CH<sub>4</sub>, 50  
15 sccm of H<sub>2</sub> at a rate of ~ 10 °C/minute followed by cooling to room temperature under 500 sccm  
16 of Ar while the base pressure is ramped to 760 Torr (Supplementary Fig. 8a). Graphene is  
17 transferred to the receiving substrates by coating one side of the Cu foil with a bilayer of PMMA  
18 (495 K A2 and 950 K A4) (Supplementary Fig. 8b-i). Each layer of PMMA is coated at 3000  
19 rpm followed by a 200 °C bake for 2 min. The backside graphene is removed by O<sub>2</sub> plasma  
20 etching prior to etching the Cu foil (Supplementary Fig. 8b-ii) in etchant overnight (Transcene  
21 CE-100). The resultant PMMA/graphene film is transferred to a 10% HCl in deionized (DI)  
22 water solution to remove residual metal particles followed by a second DI rinse (Supplementary  
23 Fig. 8b-iii). The film is then transferred onto the receiving substrate (Supplementary Fig. 8b-iv)



1 with predefined FIB holes ( $\sim 300$  nm in diameter) and PMMA is removed in a 1:1 methylene  
2 chloride/methanol solution for 30 min. The samples undergo a  $400$  °C anneal under Ar (500  
3 sccm) and  $H_2$  (100 sccm) flow to remove residual PMMA.

#### 4 **Raman Spectroscopy and AFM Characterization:**

5 Raman mapping is performed using a scanning confocal Renishaw Raman microscope (inVia and  
6 WiRE 3.2 software). Data is collected using a 633 nm edge emitting laser (laser spot size  $\sim 1.3$   
7  $\mu\text{m}$  and  $\sim 0.1$  mW incident power), a  $50\times$  long working distance objective, a 1800 lines/mm  
8 grating, and 30 s acquisition time. 121 spectra is collected over  $20 \times 20 \mu\text{m}^2$  area at a  $2 \mu\text{m}$  step  
9 size and analyzed by fitting mixed Gaussian and Lorentzian curves around the D, G, and 2D  
10 Raman peaks centered at  $\approx 1340$ ,  $1590$ , and  $2660 \text{ cm}^{-1}$ , respectively. A cubic spline interpolation  
11 is used to subtract the background before curve fitting. Atomic force microscope (AFM) data is  
12 collected using a Digital Instruments Dimension 3000 AFM in a tapping mode. Calculated root-  
13 mean-square (RMS) roughness values are obtained using Nanoscope Analysis v.1.4 software  
14 from Bruker Corporation. Three dimensional images are rendered using Gwyddion AFM  
15 analysis software.

#### 16 **Supporting Membranes:**

17 Membranes consisting of stacked layers of  $Al_2O_3$  and  $SiN_x$  is fabricated on  $300 \pm 2 \mu\text{m}$  thick  
18 double-side polished  $\langle 100 \rangle$  silicon wafers purchased from Silicon Quest International. Wafers  
19 are piranha cleaned (1:1  $H_2SO_4:H_2O_2$ ) for 15 minutes before depositing  $Al_2O_3$  *via* ALD  
20 (Cambridge Nanotech). 50 nm of  $Al_2O_3$  was deposited at a platen temperature of  $250$  °C using  
21 tetramethyl-aluminum (TMA) and water vapor precursors. Subsequently, 200 nm of low-stress  
22  $SiN_x$  is deposited (STS Mesc PECVD System) using a mixed-frequency recipe (High Frequency:  
23 6 s at 13.56 MHz, platen power of 20 W and Low Frequency: 2 s at 380 kHz, platen power of 60

1  
2  
3 1 W) with precursors  $\text{SiH}_4$  and  $\text{NH}_3$  at flow rates of 40 sccm and 55 sccm, respectively, at a platen  
4  
5 2 temperature of 300 °C. Another 50 nm of  $\text{Al}_2\text{O}_3$  (ALD) is deposited with the same parameters as  
6  
7 3 described before. Optical lithography is used to define 80  $\mu\text{m}$  square windows on the back of the  
8  
9 4 wafer with the aid of plasma resistant Megaposit SPR-220 photoresist and an ABM Flood  
10  
11 5 Exposure (Model 60) tool. The wafer is then placed inside a STS Pegasus ICP DRIE and 80  $\mu\text{m}$   
12  
13 6 square membranes are suspended using a Bosch etching process. 300 to 350 nm holes are then  
14  
15 7 formed in these membranes using a focused ion beam (FIB) (FEI DB235) operated at a beam  
16  
17 8 current of 30 pA.  
18  
19  
20  
21

### 22 9 **Nanopore Fabrication and Nanopore Fluidic Measurement**

23  
24 10 The graphene- $\text{Al}_2\text{O}_3$ -graphene- $\text{Al}_2\text{O}_3$  stack is fabricated sequentially using the same graphene  
25  
26 11 transfer and ALD process as described previously. The thickness of  $\text{Al}_2\text{O}_3$  for both dielectric  
27  
28 12 layers is 24 nm. A seed layer Al (2nm thick) is deposited on graphene using a CHA SEC-600  
29  
30 13 electron-beam evaporator prior to deposition of both dielectric layers. The second (top) graphene  
31  
32 14 layer is contacted with Ti/Au contacts. Electrical contacts, Ti (2 nm thickness adhesion layer)  
33  
34 15 and Au (300 nm thick), are deposited onto G2 by shadow masking and e-beam evaporation. The  
35  
36 16 measured sheet resistance of graphene is 6.7  $\text{k}\Omega/\square$ . Single nanopores of 5-20 nm diameter are  
37  
38 17 drilled in the graphene-embedded membrane using a JOEL 2010F field-emission gun TEM  
39  
40 18 operated at 200 kV in CBED mode with focused electron probe of diameter = 1.6 nm.  $\text{O}_2$  plasma  
41  
42 19 treatment at 50 W for 30 sec on source side facilitates wetting. Subsequently Al wires are  
43  
44 20 attached on Ti/Au contacts using silver paint and the chip is assembled in a custom-built  
45  
46 21 chamber. Ethanol is filled in both reservoirs initially to promote wetting. Subsequently the  
47  
48 22 ethanol is flushed out and the reservoirs are filled with a solution of 1 M KCl, 10 mM Tris, 1  
49  
50  
51  
52  
53  
54  
55  
56  
57  
58  
59  
60

1 mM EDTA at pH 7.6. All nanopore experiments are performed with Axopatch 200B and Digidata 1440A at room temperature ( $22 \pm 2$  °C).

### 3 Electrostatic Simulations

4 The mathematical model for ion transport involves a set of equations governing ionic transport and the electric potential.<sup>56</sup>

6 The total flux due to diffusion and electromigration of the *ith* species (ions) is given by the following expression

$$\mathbf{\Gamma}_i = -D_i \nabla c_i - \frac{D_i}{RT} z_i F c_i \nabla \phi \quad (3)$$

9 where  $F$  is the Faraday's constant,  $z_i$  is the valence,  $D_i$  is the diffusion coefficient,  $\mathbf{\Gamma}_i$  is the flux,  $c_i$  is the concentration of the *ith* species, and  $\phi$  is the electrical potential. The Nernst-Planck (NP) equation describes the reaction rate ( $r_i$ ) of dissolved species.

$$\frac{\partial c_i}{\partial t} = -\nabla \cdot \mathbf{\Gamma}_i + r_i \quad (4)$$

13 The electrical potential distribution is governed by the Poisson equation

$$\nabla \cdot (\epsilon_r \nabla \phi) = -\frac{F \sum z_i c_i}{\epsilon_0} \quad (5)$$

15 where  $\epsilon_0$  is the permittivity of vacuum and  $\epsilon_r$  is the relative permittivity. The electric potential at the wall surface is governed by

$$\frac{\partial \phi}{\partial n} = -\frac{\sigma_s}{\epsilon_0 \epsilon_r} \quad (6)$$

18 where  $\sigma_s$  is the surface charge density and  $n$  is the normal to the wall.

1  
2  
3 1 The Poisson-Nernst-Planck equations (PNP) equations can be simplified by integrating equation  
4  
5  
6 2 (3) and (5) across the channel, which gives

$$7 \quad \frac{\partial \bar{c}_i}{\partial t} = \frac{1}{A} \frac{\partial}{\partial x} \left( AD_i \frac{\partial \bar{c}_i}{\partial x} + A \frac{D_i}{RT} z_i F \bar{c}_i \frac{\partial \bar{\phi}}{\partial x} \right) + \bar{r}_i \quad (7)$$

8  
9  
10  
11  
12  
13 4 and

$$14 \quad \frac{\partial}{\partial x} \left( A \frac{\partial \bar{\phi}}{\partial x} \right) = - \frac{A \left( F \sum z_i \bar{c}_i + 4\sigma_s / d \right)}{\epsilon_r \epsilon_0} \quad (8)$$

15  
16  
17  
18  
19  
20  
21  
22 6  
23  
24 7 where  $A$  is the cross-sectional area,  $x$  is the coordinate along the channel,  $d$  is the nanopore  
25  
26  
27 8 diameter,  $\bar{c}_i$ ,  $\bar{r}_i$ ,  $\bar{\phi}$  are the cross-sectional averaged concentration, reaction rate, and electric  
28  
29  
30 9 potential, respectively.

31  
32  
33 10 From equation (7) and (8), we obtain the cross-sectional averaged electric potential, and ionic  
34  
35 11 concentration. The drain current is calculated by multiplying the current density along the  $x$   
36  
37 12 direction (assumed normal to pore wall) with the cross-sectional area at drain.

$$38 \quad I_x = \sum_i z_i F \Gamma_{xi} \quad (9)$$

39  
40  
41  
42  
43  
44 14 where  $\Gamma_{xi}$  is the flux rate of  $i$ th species in the  $x$  direction.

45  
46  
47 15 The gate current is calculated from the reaction rate of the species near the graphene gate. The  
48  
49 16 oxidation rate of  $\text{Cl}^-$  is assumed as a function of the electrical potential bias and the local  
50  
51 17 concentration.

$$52 \quad \bar{r}_{\text{Cl}^-} = -r_{0\text{Cl}^-} \left[ \exp(aV_G - bV_D) - 1 \right] \bar{c}_{\text{Cl}^-} \quad (10)$$

1 where  $r_{0Cl^-}$ ,  $a$  and  $b$  are fitting parameters.  $\bar{c}_{Cl^-}$  is the cross-sectional averaged concentration of  
 2  $Cl^-$  at pore surface (mM or mole/m<sup>3</sup>).

3 Near the graphene gate edge, water oxidation, which generated  $H^+$  ions.



5 The generation rate of  $H^+$  is assumed as

$$6 \quad \bar{r}_{H^+} = -r_{0H^+} [\exp(aV_G - bV_D) - 1] \quad (12)$$

7 The gate current  $I_G$  is calculated from

$$8 \quad I_G = \frac{\pi}{4} d^2 l_r F (\bar{r}_{H^+} - \bar{r}_{Cl^-}) \quad (13)$$

9 where  $l_r$  is the length of reaction region. In the simulations,  $l_r$  is taken as 2nm,  $r_{0Cl^-} = 5 \times 10^7 \text{ s}^{-1}$ ,  
 10 and  $r_{0H^+} = 2 \times 10^7 \text{ mol/m}^3/\text{s}$ . The parameters  $a$  and  $b$  are correlated to the pore size and  
 11 electrolyte concentrations. In these simulations,  $d > \kappa^{-1}$  where  $\kappa^{-1}$  is the debye layer thickness, we  
 12 choose  $a = 0.66 \text{ V}^{-1}$ , and  $b = 2.05 \text{ V}^{-1}$ . However when  $d < \kappa^{-1}$ , for  $d = 5\text{nm}$  and KCl concentration  
 13 of 10 mM, we choose  $a = 0.625 \text{ V}^{-1}$ , and  $b = 1.25 \text{ V}^{-1}$ . The gate current from water oxidation is  
 14 much smaller than that from  $Cl^-$  oxidation. However water oxidation induces  $H^+$  ions in the  
 15 nanopore, which affects the surface charge density of the  $Al_2O_3$  layer.

16 The surface charge density of the  $Al_2O_3$  layer is determined by the density difference of the sites  
 17 attracting positive and negative charges.

$$18 \quad \sigma_s = e(N_+ - N_-) \quad (14)$$

$$19 \quad N = N_+ + N_- + N_0 \quad (15)$$

1 where  $N_+$ ,  $N_-$ , and  $N_0$  are the density of positively charged, negatively charged, and neutral sites,  
 2 respectively.

3 The densities of the positively and negatively charged sites are related to the pH value and  
 4 surface potential  $\psi_s$ .<sup>57</sup>

$$\frac{N_+ N_0^{ISP}}{N_+^{ISP} N_0} = \frac{\bar{c}_{H^+}}{c_{H^+}^{ISP}} \exp\left(-\frac{F\psi_s}{RT}\right) \quad (16)$$

$$\frac{N_- N_0^{ISP}}{N_-^{ISP} N_0} = \frac{c_{H^+}^{ISP}}{\bar{c}_{H^+}} \exp\left(\frac{F\psi_s}{RT}\right) \quad (17)$$

7 where ISP is the isoelectric point,  $c_{H^+}$  is the  $H^+$  concentration in the nanopore. The surface  
 8 charge density is obtained by the Grahame equation.<sup>34</sup>

$$\sigma_s = \epsilon_r \epsilon_0 \frac{RT}{zF} \kappa \sinh\left(\frac{F\psi_s}{2RT}\right) \quad (18)$$

10 Given  $N$ ,  $c_{H^+}^{ISP}$ , and  $N_0^{ISP}$ , the surface charge density can be obtained by solving equations  
 11 (14)-(18). In the simulations,  $c_{H^+}^{ISP}$  is chosen as  $10^{-8}$  mM,  $N = 6$  /nm<sup>2</sup>, and  $N_0^{ISP} = 2$  /nm<sup>2</sup>. We  
 12 calculate  $\bar{c}_{H^+} = 0.01$  mM in a 5 nm pore (for  $V_{ds} = -500$  mV and  $V_{gs} = 500$  mV). We also  
 13 calculate  $\bar{c}_{Cl^-} = 5000$  mM and  $\bar{c}_{Cl^-} = 8500$  mM for 10mM and 1000mM KCl solutions  
 14 respectively.

## 15 Acknowledgements

16 The authors would like to acknowledge support from the National Institutes of Health (R21  
 17 CA155863) and Oxford Nanopore Technologies, U.K for supporting the effort. D. Estrada and E.

1 Pop acknowledge support from the National Science Foundation (NSF) Graduate Research  
2 Fellowship Program and CAREER award ECCS 09-54423, respectively.

### 3 **Supporting Information**

4 Leakage studies, additional graphene electrochemical studies, photographs of experimental  
5 setup, characterization of graphene transfer process and dielectric deposition. This material is  
6 available free of charge *via* the Internet at <http://pubs.acs.org>

### 7 **References**

- 8 1. Novoselov, K. S.; Geim, A. K.; Morozov, S. V.; Jiang, D.; Zhang, Y.; Dubonos, S. V.;  
9 Grigorieva, I. V.; Firsov, A. A., Electric Field Effect in Atomically Thin Carbon Films. *Science* **2004**,  
10 *306*, 666-669.
- 11 2. Bolotin, K. I.; Sikes, K. J.; Jiang, Z.; Klima, M.; Fudenberg, G.; Hone, J.; Kim, P.; Stormer, H.  
12 L., Ultrahigh Electron Mobility in Suspended Graphene. *Solid State Commun.* **2008**, *146*, 351-  
13 355.
- 14 3. Balandin, A. A., Thermal Properties of Graphene and Nanostructured Carbon Materials.  
15 *Nat. Mater.* **2011**, *10*, 569-581.
- 16 4. Mak, K. F.; Shan, J.; Heinz, T. F., Electronic Structure of Few-Layer Graphene:  
17 Experimental Demonstration of Strong Dependence on Stacking Sequence. *Phys. Rev. Lett.*  
18 **2010**, *104*, 176404.
- 19 5. Pumera, M., Electrochemistry of Graphene: New Horizons for Sensing and Energy  
20 Storage. *Chem. Rec.* **2009**, *9*, 211-223.
- 21 6. Hou, J.; Shao, Y.; Ellis, M. W.; Moore, R. B.; Yi, B., Graphene-Based Electrochemical  
22 Energy Conversion and Storage: Fuel Cells, Supercapacitors and Lithium Ion Batteries. *Phys.*  
23 *Chem. Chem. Phys.* **2011**, *13*, 15384-15402.
- 24 7. Shao, Y.; Wang, J.; Wu, H.; Liu, J.; Aksay, I. A.; Lin, Y., Graphene Based Electrochemical  
25 Sensors and Biosensors: A Review. *Electroanalysis* **2010**, *22*, 1027-1036.
- 26 8. Brownson, D. A.; Banks, C. E., Graphene Electrochemistry: An Overview of Potential  
27 Applications. *The Analyst* **2010**, *135*, 2768-2778.
- 28 9. Banks, C. E.; Davies, T. J.; Wildgoose, G. G.; Compton, R. G., Electrocatalysis at Graphite  
29 and Carbon Nanotube Modified Electrodes: Edge-Plane Sites and Tube Ends Are the Reactive  
30 Sites. *Chem. Commun. (Cambridge, U.K.)* **2005**, 829-841.
- 31 10. Durkan, C.; Welland, M. E., Analysis of Failure Mechanisms in Electrically Stressed Gold  
32 Nanowires. *Ultramicroscopy* **2000**, *82*, 125-133.
- 33 11. Behnam, A.; Lyons, A. S.; Bae, M.-H.; Chow, E. K.; Islam, S.; Neumann, C. M.; Pop, E.,  
34 Transport in Nanoribbon Interconnects Obtained from Graphene Grown by Chemical Vapor  
35 Deposition. *Nano Lett.* **2012**, *12*, 4424-4430.

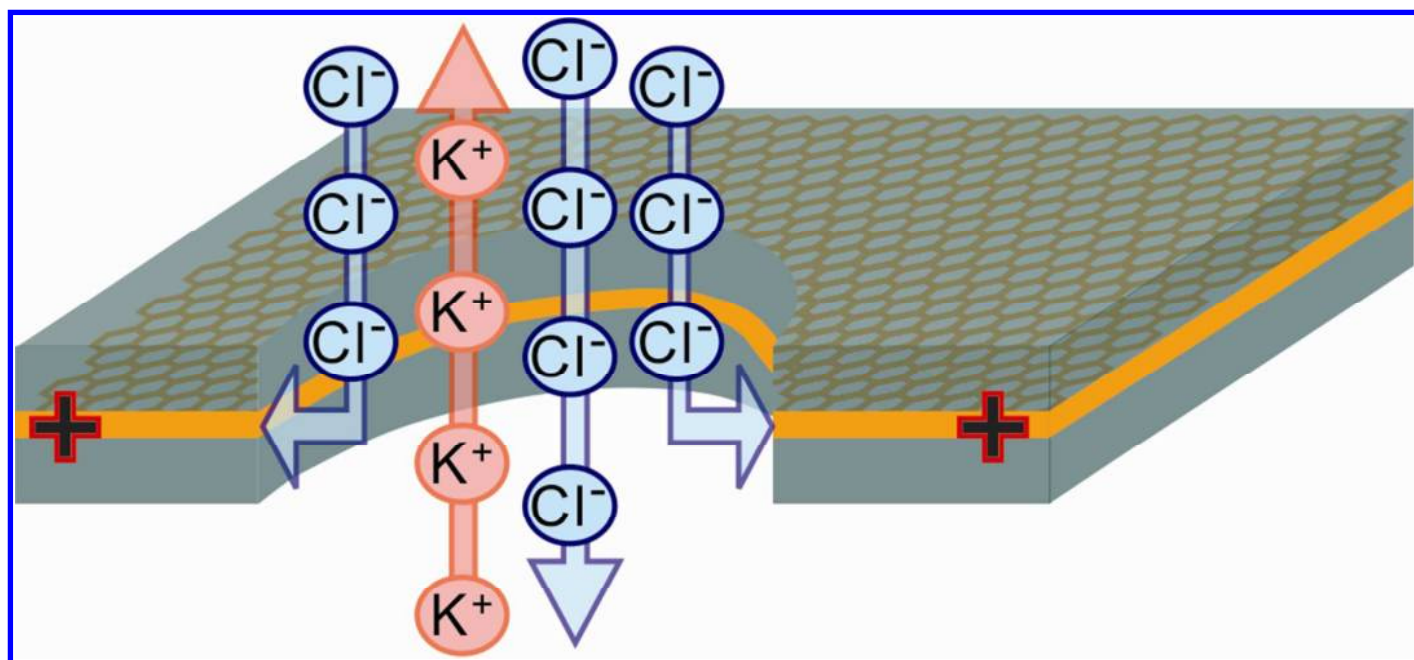
12. Ambrosi, A.; Bonanni, A.; Pumera, M., Electrochemistry of Folded Graphene Edges. *Nanoscale* **2011**, *3*, 2256-2260.
13. Davies, T. J.; Hyde, M. E.; Compton, R. G., Nanotrench Arrays Reveal Insight into Graphite Electrochemistry. *Angew. Chem., Int. Ed. Engl.* **2005**, *44*, 5121-5126.
14. Zhou, M.; Zhai, Y.; Dong, S., Electrochemical Sensing and Biosensing Platform Based on Chemically Reduced Graphene Oxide. *J. Anal. Chem.* **2009**, *81*, 5603-5613.
15. Liu, C.; Yu, Z.; Neff, D.; Zhamu, A.; Jang, B. Z., Graphene-Based Supercapacitor with an Ultrahigh Energy Density. *Nano Lett.* **2010**, *10*, 4863-4868.
16. Yoo, J. J.; Balakrishnan, K.; Huang, J.; Meunier, V.; Sumpter, B. G.; Srivastava, A.; Conway, M.; Reddy, A. L.; Yu, J.; Vajtai, R., *et al.*, Ultrathin Planar Graphene Supercapacitors. *Nano Lett.* **2011**, *11*, 1423-1427.
17. Girit, Ç. Ö.; Meyer, J. C.; Erni, R.; Rossell, M. D.; Kisielowski, C.; Yang, L.; Park, C.-H.; Crommie, M. F.; Cohen, M. L.; Louie, S. G., *et al.*, Graphene at the Edge: Stability and Dynamics. *Science* **2009**, *323*, 1705-1708.
18. Merchant, C. A.; Healy, K.; Wanunu, M.; Ray, V.; Peterman, N.; Bartel, J.; Fischbein, M. D.; Venta, K.; Luo, Z.; Johnson, A. T., *et al.*, DNA Translocation through Graphene Nanopores. *Nano Lett.* **2010**, *10*, 2915-2921.
19. Schneider, G. F.; Kowalczyk, S. W.; Calado, V. E.; Pandraud, G.; Zandbergen, H. W.; Vandersypen, L. M.; Dekker, C., DNA Translocation through Graphene Nanopores. *Nano Lett.* **2010**, *10*, 3163-3167.
20. Zhang, Y.; Zhang, B.; White, H. S., Electrochemistry of Nanopore Electrodes in Low Ionic Strength Solutions. *J. Phys. Chem. B* **2006**, *110*, 1768-1774.
21. Venkatesan, B. M.; Estrada, D.; Banerjee, S.; Jin, X.; Dorgan, V. E.; Bae, M.-H.; Aluru, N. R.; Pop, E.; Bashir, R., Stacked Graphene-Al<sub>2</sub>O<sub>3</sub> Nanopore Sensors for Sensitive Detection of DNA and DNA-Protein Complexes. *ACS Nano* **2011**, *6*, 441-450.
22. Liang, X.; Sperling, B. A.; Calizo, I.; Cheng, G.; Hacker, C. A.; Zhang, Q.; Obeng, Y.; Yan, K.; Peng, H.; Li, Q., *et al.*, Toward Clean and Crackless Transfer of Graphene. *ACS Nano* **2011**, *5*, 9144-9153.
23. Lenski, D. R.; Fuhrer, M. S., Raman and Optical Characterization of Multilayer Turbostratic Graphene Grown *Via* Chemical Vapor Deposition. *J. Appl. Phys.* **2011**, *110*.
24. Salehi-Khojin, A.; Estrada, D.; Lin, K. Y.; Bae, M.-H.; Xiong, F.; Pop, E.; Masel, R. I., Polycrystalline Graphene Ribbons as Chemiresistors. *Adv. Mater.* **2012**, *24*, 53-57.
25. Kim, S.; Nah, J.; Jo, I.; Shahrjerdi, D.; Colombo, L.; Yao, Z.; Tutuc, E.; Banerjee, S. K., Realization of a High Mobility Dual-Gated Graphene Field-Effect Transistor with Al<sub>2</sub>O<sub>3</sub> Dielectric. *Appl. Phys. Lett.* **2009**, *94*, 062107.
26. Wang, L.; Travis, J. J.; Cavanagh, A. S.; Liu, X.; Koenig, S. P.; Huang, P. Y.; George, S. M.; Bunch, J. S., Ultrathin Oxide Films by Atomic Layer Deposition on Graphene. *Nano Lett.* **2012**, *12*, 3706-3710.
27. Venkatesan, B. M.; Dorvel, B.; Yemenicioglu, S.; Watkins, N.; Petrov, I.; Bashir, R., Highly Sensitive, Mechanically Stable Nanopore Sensors for DNA Analysis. *Adv. Mater.* **2009**, *21*, 2771-2776.



- 1  
2  
3  
4  
5  
6  
7  
8  
9  
10  
11  
12  
13  
14  
15  
16  
17  
18  
19  
20  
21  
22  
23  
24  
25  
26  
27  
28  
29  
30  
31  
32  
33  
34  
35  
36  
37  
38  
39  
40  
41  
42  
43  
44  
45  
46  
47  
48  
49  
50  
51  
52  
53  
54  
55  
56  
57  
58  
59  
60
- 1 28. Chen, P.; Mitsui, T.; Farmer, D. B.; Golovchenko, J.; Gordon, R. G.; Branton, D., Atomic  
2 Layer Deposition to Fine-Tune the Surface Properties and Diameters of Fabricated Nanopores.  
3 *Nano Lett.* **2004**, *4*, 1333-1337.
- 4 29. Paik, K. H.; Liu, Y.; Tabard-Cossa, V.; Waugh, M. J.; Huber, D. E.; Provine, J.; Howe, R. T.;  
5 Dutton, R. W.; Davis, R. W., Control of DNA Capture by Nanofluidic Transistors. *ACS Nano* **2012**,  
6 *6*, 6767-6775.
- 7 30. Reddy, B., Jr.; Dorvel, B.; Go, J.; Nair, P.; Elibol, O.; Credo, G.; Daniels, J.; Chow, E. C.; Su,  
8 X.; Varma, M., *et al.*, High-K Dielectric Al<sub>2</sub>O<sub>3</sub> Nanowire and Nanoplate Field Effect Sensors for  
9 Improved Ph Sensing. *Biomed. Microdevices* **2011**, *13*, 335-344.
- 10 31. Wallrapp, F.; Fromherz, P., TiO<sub>2</sub> and HfO<sub>2</sub> in Electrolyte-Oxide-Silicon Configuration for  
11 Applications in Bioelectronics. *J. Appl. Phys.* **2006**, *99*, 114103.
- 12 32. Smeets, R. M. M.; Keyser, U. F.; Krapf, D.; Wu, M.-Y.; Dekker, N. H.; Dekker, C., Salt  
13 Dependence of Ion Transport and DNA Translocation through Solid-State Nanopores. *Nano Lett.*  
14 **2005**, *6*, 89-95.
- 15 33. Li, W.; Tan, C.; Lowe, M. A.; Abruña, H. c. D.; Ralph, D. C., Electrochemistry of Individual  
16 Monolayer Graphene Sheets. *ACS Nano* **2011**, *5*, 2264-2270.
- 17 34. Bard, A. J.; Faulkner, L. R., *Electrochemical Methods : Fundamentals and Applications*.  
18 2nd ed.; Wiley: New York, 2001; pp 124,546,808.
- 19 35. McCreery, R. L., Advanced Carbon Electrode Materials for Molecular Electrochemistry.  
20 *Chem. Rev.* **2008**, *108*, 2646-2687.
- 21 36. Britto, P. J.; Santhanam, K. S. V.; Rubio, A.; Alonso, J. A.; Ajayan, P. M., Improved Charge  
22 Transfer at Carbon Nanotube Electrodes. *Adv. Mater.* **1999**, *11*, 154-157.
- 23 37. Nugent, J. M.; Santhanam, K. S. V.; Rubio, A.; Ajayan, P. M., Fast Electron Transfer  
24 Kinetics on Multiwalled Carbon Nanotube Microbundle Electrodes. *Nano Lett.* **2001**, *1*, 87-91.
- 25 38. Krauss, B.; Nemes-Incze, P.; Skakalova, V.; Biro, L. P.; Klitzing, K.; Smet, J. H., Raman  
26 Scattering at Pure Graphene Zigzag Edges. *Nano Lett.* **2010**, *10*, 4544-4548.
- 27 39. Saha, K. K.; Drndic, M.; Nikolic, B. K., DNA Base-Specific Modulation of Microampere  
28 Transverse Edge Currents through a Metallic Graphene Nanoribbon with a Nanopore. *Nano*  
29 *Lett.* **2012**, *12*, 50-55.
- 30 40. Ritter, K. A.; Lyding, J. W., The Influence of Edge Structure on the Electronic Properties  
31 of Graphene Quantum Dots and Nanoribbons. *Nat. Mater.* **2009**, *8*, 235-242.
- 32 41. Rieger, P. H., *Electrochemistry*. 2nd ed.; Chapman & Hall: New York, 1994; pp 152.
- 33 42. Liu, J.; Kvetny, M.; Feng, J.; Wang, D.; Wu, B.; Brown, W.; Wang, G., Surface Charge  
34 Density Determination of Single Conical Nanopores Based on Normalized Ion Current  
35 Rectification. *Langmuir* **2011**, *28*, 1588-1595.
- 36 43. Bockris, J. O. M.; Reddy, A. K. N., *Modern Electrochemistry*. 2nd ed.; Plenum Press: New  
37 York, 1998; pp 1234.
- 38 44. Israelachvili, J. N., *Intermolecular and Surface Forces*. 2nd ed.; Academic Press London:  
39 1991; pp 238.
- 40 45. Precision Material Modification and Patterning with He Ions. *J. Vac. Sci. Technol., B:*  
41 *Microelectron. Nanometer Struct.* **2009**, *27*, 2755.

- 1  
2  
3 1 46. Dorvel, B. R.; Reddy, B.; Go, J.; Duarte Guevara, C.; Salm, E.; Alam, M. A.; Bashir, R.,  
4 2 Silicon Nanowires with High-K Hafnium Oxide Dielectrics for Sensitive Detection of Small  
5 3 Nucleic Acid Oligomers. *ACS Nano* **2012**, *6*, 6150-6164.  
6 4 47. Fallahazad, B.; Lee, K.; Lian, G.; Kim, S.; Corbet, C. M.; Ferrer, D. A.; Colombo, L.; Tutuc,  
7 5 E., Scaling of Al<sub>2</sub>O<sub>3</sub> Dielectric for Graphene Field-Effect Transistors. *Appl. Phys. Lett.* **2012**, *100*,  
8 6 093112.  
9 7 48. Wanunu, M.; Morrison, W.; Rabin, Y.; Grosberg, A. Y.; Meller, A., Electrostatic Focusing  
10 8 of Unlabelled DNA into Nanoscale Pores Using a Salt Gradient. *Nat. Nanotechnol.* **2010**, *5*, 160-  
11 9 165.  
12 10 49. Venkatesan, B. M.; Bashir, R., Nanopore Sensors for Nucleic Acid Analysis. *Nat.*  
13 11 *Nanotechnol.* **2011**, *6*, 615-624.  
14 12 50. Huang, S.; He, J.; Chang, S.; Zhang, P.; Liang, F.; Li, S.; Tuchband, M.; Fuhrmann, A.; Ros,  
15 13 R.; Lindsay, S., Identifying Single Bases in a DNA Oligomer with Electron Tunnelling. *Nat.*  
16 14 *Nanotechnol.* **2010**, *5*, 868-873.  
17 15 51. Tsutsui, M.; Taniguchi, M.; Yokota, K.; Kawai, T., Identifying Single Nucleotides by  
18 16 Tunnelling Current. *Nat. Nanotechnol.* **2010**, *5*, 286-290.  
19 17 52. Tsutsui, M.; Rahong, S.; Iizumi, Y.; Okazaki, T.; Taniguchi, M.; Kawai, T., Single-Molecule  
20 18 Sensing Electrode Embedded in-Plane Nanopore. *Sci. Rep.* **2011**, *1*, 46.  
21 19 53. Cherf, G. M.; Lieberman, K. R.; Rashid, H.; Lam, C. E.; Karplus, K.; Akeson, M., Automated  
22 20 Forward and Reverse Ratcheting of DNA in a Nanopore at 5-Å Precision. *Nat. Biotechnol.* **2012**,  
23 21 *30*, 344-348.  
24 22 54. He, Y.; Tsutsui, M.; Fan, C.; Taniguchi, M.; Kawai, T., Controlling DNA Translocation  
25 23 through Gate Modulation of Nanopore Wall Surface Charges. *ACS Nano* **2011**, *5*, 5509-5518.  
26 24 55. Kim, R.-H.; Bae, M.-H.; Kim, D. G.; Cheng, H.; Kim, B. H.; Kim, D.-H.; Li, M.; Wu, J.; Du, F.;  
27 25 Kim, H.-S., *et al.*, Stretchable, Transparent Graphene Interconnects for Arrays of Microscale  
28 26 Inorganic Light Emitting Diodes on Rubber Substrates. *Nano Lett.* **2011**, *11*, 3881-3886.  
29 27 56. Karniadakis, G.; Beskök, A.; Aluru, N. R., *Microflows and Nanoflows : Fundamentals and*  
30 28 *Simulation*. Springer: New York, NY, 2005; pp 255-304.  
31 29 57. Mustafa, S.; Dilara, B.; Neelofer, Z.; Naeem, A.; Tasleem, S., Temperature Effect on the  
32 30 Surface Charge Properties of  $\gamma$ -Al<sub>2</sub>O<sub>3</sub>. *J. Colloid Interface Sci.* **1998**, *204*, 284-293.  
33  
34  
35  
36  
37  
38  
39  
40  
41  
42  
43  
44  
45  
46  
47  
48  
49  
50  
51  
52  
53  
54  
55  
56  
57  
58  
59  
60

37 **Table of content graphic**



1

2